PHYSICAL REVIEW B **89**, 205406 (2014)

Dissociative adsorption of O_2 on unreconstructed metal (100) surfaces: Pathways, energetics, and sticking kinetics

Da-Jiang Liu
Ames Laboratory—USDOE, Iowa State University, Ames, Iowa 50011, USA

James W. Evans
Ames Laboratory—USDOE, Iowa State University, Ames, Iowa 50011, USA
and Department of Physics & Astronomy, Iowa State University, Ames, Iowa 50011, USA

(Received 2 December 2013; revised manuscript received 15 April 2014; published 6 May 2014)

An accurate description of oxygen dissociation pathways and kinetics for various local adlayer environments is key for an understanding not just of the coverage dependence of oxygen sticking, but also of reactive steady states in oxidation reactions. Density functional theory analysis for $M(100)$ surfaces with $M =$ Pd, Rh, and Ni, where O prefers the fourfold hollow adsorption site, does not support the traditional Brundle-Behm-Barker picture of dissociative adsorption onto second-nearest-neighbor hollow sites with an additional blocking constraint. Rather adsorption via neighboring vicinal bridge sites dominates, although other pathways can be active. The same conclusion also applies for $M =$ Pt and Ir, where oxygen prefers the bridge adsorption site. Statistical mechanical analysis is performed based on kinetic Monte Carlo simulation of a multisite lattice-gas model consistent with our revised picture of adsorption. This analysis determines the coverage and temperature dependence of sticking for a realistic treatment of the oxygen adlayer structure.

DOI: 10.1103/PhysRevB.89.205406 PACS number(s): 68.43.−h, 82.37.Np, 31.15.E−, 05.90.+m

I. INTRODUCTION

Numerous experimental studies have assessed the dependence on oxygen coverage θ_O of the sticking coefficient $S(\theta_O)$ for dissociative oxygen adsorption on various metal (100) surfaces [1–12]. Analysis of this behavior can provide insight into the underlying dissociation mechanism. For example, early studies of oxygen adsorption on Ni(100) [1,2] suggested an effective saturation coverage of about $\theta_O^S = 0.25$ monolayers (ML) which prompted development of the so-called Brundle-Behm-Barker eight-site model [2,13]. In this model, which was showcased in Zangwill's monograph on surface physics [14], the oxygen molecule dissociates on diagonally neighboring fourfold hollow adsorption sites provided the six neighbors to these are free of O [2]. This latter constraint blocks adsorption on a perfectly ordered 0.25 ML $p(2 \times 2)$-O adlayer which develops on Ni(100). However, we should caution that a later study [3] for Ni(100) claimed a significantly higher θ_O^S, which might bring into question the appropriateness of the model. The eight-site model was also applied for oxygen adsorption on Pd(100) [4,5,15–17].

Setting aside the issue of validity of the eight-site model, development of this type of environment-dependent adsorption model is essential for realistic statistical mechanical modeling of $S(\theta_O)$. Specification of the sticking dynamics for any local adsorbate environment might be described as incorporating "dynamic heterogeneity" in adsorption [18] into the model. In addition, such modeling should also incorporate a realistic description of adlayer structure and ordering [17,19]. For higher surface temperature (T) where the adlayer is equilibrated, its structure is characterized by a Gibbs ensemble which is determined by adspecies adsorption and interaction energies. Then $S(\theta_O)$ is uniquely determined by these interactions, by T, and by the adsorption rule. At lower T, there may be kinetically limited ordering [4,18] in which case $S(\theta_O)$ reflects the entire history of the adsorption process. Perhaps even more significantly, these types of oxygen adsorption models are also essential for comprehensive and realistic statistical mechanical modeling of reactive steady states in oxidation reactions [17,19]. We emphasize that these nonequilibrium steady states for given reactant partial pressures and T are determined not just by the thermodynamics of the relevant mixed reactant adlayers, but also by the dynamics of adsorption, desorption, and reaction [20].

The potential for developing such realistic adsorption models is greatly facilitated by the availability of density functional theory (DFT) analysis of energetics [21,22]. Indeed, several such studies have considered O_2 adsorption on clean metal (100) and (111) surfaces; see, e.g., Refs. [23–26]. A central focus has been on determination of the mechanism of energy loss for adsorption on a clean surface, and also on assessing possible hot-adatom mobility due to inefficient energy transfer. One study of particular relevance here, of O_2 adsorption on Pd(100) [23], focused on electronically nonadiabatic behavior showing weak 100 meV energy transfer due to electron-hole excitation during the dissociation process. Interestingly, hot-adatom motion was proposed for this system based on an early statistical mechanical analysis of experimental surface diffraction data, but utilizing a simple eight-site model [5]. Other studies have begun to consider the effect of preadsorbed oxygen of the dissociation barrier for oxygen, at least on Pt(111) surfaces [27,28].

The central focus of this work is on the development of local-environment-dependent adsorption models for dissociative adsorption of oxygen on a broad range of unreconstructed metal (100) [$M(100)$] surfaces, with $M =$ Pd, Rh, Pt, Ni, and Ir. This is achieved with the aid of extensive DFT analysis for adsorption not just on clean surfaces, but also on partly covered surfaces. (Limited results have been presented in Ref. [20] just for Pd and Rh.) The resulting insights are integrated into a statistical mechanical multisite lattice-gas model for a complete characterization of sticking kinetics.

This model incorporates a comprehensive set of oxygen adsorption and lateral interaction energies mostly determined previously [20], and its behavior is assessed via kinetic Monte Carlo simulations. The resulting picture of adsorption is quite distinct from that of the eight-site model. Instead, the dominant adsorption pathway involves nearest-neighbor (NN) vicinal bridge sites, a feature common to all the above metals.

II. DFT STUDIES OF O_2 ON Pd, Rh, Ni, Pt, AND Ir(100) SURFACES

The results presented below are from DFT calculations performed using the plane-wave VASP code [29] for slab geometries representing the metal surface with the Perdew-Burke-Ernzerhof (PBE) [30] exchange-correlation functional. The projector augmented wave method [31] is used for computational efficiency. Molecules are adsorbed on one side of the slab, and induced artificial dipole interactions are corrected using the method of Neugebauer and Scheffler [32]. The energy cutoff for the plane-wave basis set is 400 eV, and the k-point grid is $(6 \times 6 \times 1)$ for (2×2) supercells, and $(4 \times 4 \times 1)$ for $(2\sqrt{2} \times 2\sqrt{2})R45^\circ$ supercells used below. Often results for energies are averaged over the slab thickness from five to nine layers (or three to five layers for spin-polarized calculations), as this has been shown effective in reducing the influence of quantum size effects due to small slab thickness [33]. Note that for the precise calculations of adsorption and lateral interaction energies for atomic oxygen which are reported in the Appendix A, much larger supercells and thicker slabs are used. The bottom layer of the metal substrate is fixed at the bulk position, and all other atoms are free to relax.

Finally, we emphasize that for the analysis of O_2 adsorption and sticking in this paper, our focus is on the regime where a lattice-gas description of adsorbed O is appropriate. Specifically, subsequent to dissociation, oxygen adatoms occupy well-defined high-symmetry adsorption sites, where the preferred sites for various metal surfaces are well known from previous studies. This scenario generally applies for oxygen coverages below about 0.5 ML where surface reconstruction and oxidation are not present. Consequently, for the various dissociation paths considered below, one can readily deduce the final state of the dissociated atoms at preferred adsorption sites. One caveat is that dissociation may be a two-stage two-time-scale process where the adatoms first reach nearby preferred adsorption sites, and then separate further via thermal hopping to reduce repulsive adatom interactions. The latter process is captured by our statistical mechanical modeling.

A. Molecular adsorption

In the following, we consider some natural high-symmetry adsorption configurations for O_2 molecules on metal (100) surfaces. One can categorize these configurations first by the position of the center of the impinging oxygen dimer, and second by its orientation. The center of a dimer can be above a fourfold hollow (4fh) site (H), a bridge (br) site (B), or a top site (T). In each case, the dimer can be vertical (Hv, Bv, and Tv) relative to the surface plane, or flat with the dimer axis aligned along a high-symmetry [011] close-packed direction (Hx, Bx or By, and Tx), or flat with the dimer rotated diagonally 45° from the [011] direction (Hd, Bd, and Td). See Fig. 1 for an illustration for flat-lying dimer configurations. Note that unlike Hd and Td, Bd does not possess any rotational symmetry, and therefore does not correspond to any extremal point in the energy landscape. Consequently, it is not studied systematically in this work. On the other hand, there are two nonequivalent flat B configurations, one with the O atoms pointing towards two NN 4fh sites (vicinal) (Bx), and the other with the O atoms pointing towards two NN top sites (By).

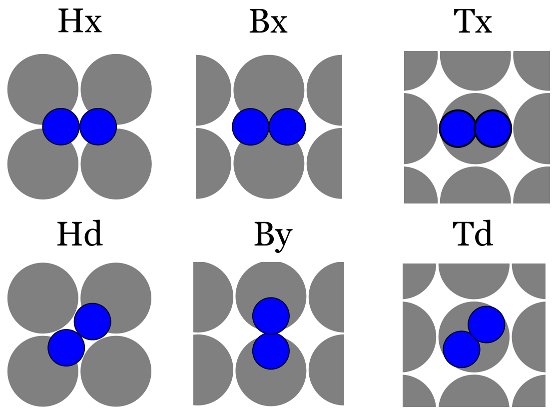

FIG. 1. (Color online) Illustration of six types of flat-lying dimer configurations on metal (100) surfaces.

Table I lists the adsorption energy (per atom in eV) of an undissociated O_2 dimer on Pd(100), Rh(100), Pt(100), and Ir(100). Results are obtained from averaging calculations using slab thickness from three to five layers. For some configurations [Hv on Rh(100), Pt(100), and Ir(100), Hd and Bx on Ir(100)], the nondissociated state is not metastable, i.e., the dimer can dissociate without any energy barrier. For these configurations, the adsorption energies are calculated by fixing the distance between the two O atoms at $0.56a$, where a is the surface lattice constant of the (100) substrate.

Table I shows that Hx is generally the most stable molecular adsorption configuration, followed by By. The relative stability of By and Bx is somewhat surprising. For By, two O atoms are close to the top sites, which are not favorable adsorption sites for atomic oxygen adsorption compared with 4fh and bridge sites, while for Bx, atoms are closer to the 4fh sites, which are the more favorable adsorption sites for atomic oxygen adsorption. This fact is quite relevant for the study of O_2 dissociation. For surfaces where 4fh sites are the most favorable adsorption sites for O (Pd, Rh, and Ni), the simplest traditional model for dissociative adsorption requires an empty NN pair of 4fh sites. Hence, we find that the Bx "starting configuration" on the natural pathway for dissociative adsorption in this model is actually not particularly favorable. The refined eight-site model assumes that O_2 dissociates to a diagonal or second-NN (2NN) pair of 4fh sites. In this case, Td is the natural starting configuration, but again DFT shows that this configuration is not very favorable. These surprising results indicate that further studies of the dissociative adsorption pathways and energetics are necessary for elucidation of O_2 adsorption on metal(100) surfaces. In Secs. II B and II C, we present

TABLE I. Energies (in eV) per atom for O_2 molecular adsorption on the (unreconstructed) (100) surface of Pd, Rh, Pt, and Ir. A negative value represents exothermic adsorption. Results are obtained from calculations on (2 × 2) supercells, averaging over slab thickness from three to five layers, using spin-polarized DFT. Numbers in italics are obtained from restrained energy optimization by fixing the distance between the two O at $0.56a$, where a is the (theoretical) surface lattice constant of the substrate, 2.80 Å (Pd), 2.72 Å (Rh), 2.81 Å (Pt), and 2.74 Å (Ir). For Pt(100), some of the configurations, which are denoted by n.m., have no metastable adsorption states.

	Hv	Hx	Hd	Bv	Bx	By	Tv	Tx	Td
Pd(100)	−0.174	−0.758	−0.315	−0.188	−0.039	−0.532	−0.022	−0.043	−0.071
Rh(100)	−0.338	*−1.195*	−0.622	−0.344	−0.388	−0.875	−0.133	−0.259	−0.382
Pt(100)	n.m.	*−0.749*	−0.132	−0.070	n.m.	−0.564	n.m.	n.m.	0.089
Ir(100)	−0.082	*−1.137*	*−0.477*	−0.207	*−0.144*	−0.900	−0.032	−0.152	−0.279

DFT results of some representative high-symmetry cuts of the potential energy surface (PES) of O_2 dissociation.

Next, we briefly discuss the magnetic properties of oxygen adsorption (noting that the above results are obtained from spin-polarized DFT calculations). The molar magnetic susceptibility of Pd, Rh, Pt, and Ir is 540, 102, 193, and 25, respectively (in units of 10^{-6} cm^3 mol^{-1}). Applying the PBE [30] approximation to the bulk Pd system yields a spurious magnetic moment of $0.3\mu_B$ at the theoretical equilibrium lattice size (3.94 Å). The spurious magnetic moment is lowered to about $0.2\mu_B$ using the PBEsol functional [34] (with theoretical lattice constant of 3.87 Å), and vanishes using the local density approximation (with theoretical lattice constant of 3.84 Å). This is consistent with results of Alexandre *et al.* [35] regarding the relationship of the magnetic moment and lattice constants of bulk Pd.

It is well known that the ground state of the oxygen molecule in vacuum is the paramagnetic triplet state, while that of the adsorbed oxygen atoms generally is singlet with zero magnetic moment [25]. Previous studies [24] have shown that *molecularly* adsorbed oxygen can have different magnetic properties, depending on the configuration. As a general rule, the higher the molecule is above the surface, the more likely it has a paramagnetic ground state. For O_2 on Rh(100), the Bv, Tv, Tx, and Td configurations are paramagnetic. On Pt(100), all except the (nonmetastable) Hx configurations are paramagnetic. On Ir(100), Bv, Tv, and Tx are paramagnetic. On Pd(100), however, due to the spurious magnetic moment of clean surfaces, it is not easy to distinguish the magnetic properties of adsorbed O_2 molecules. However, by comparing the (absolute) magnetic moments of the clean and O_2 adsorbed surfaces, one can conclude that Bx, Tx, and Td increase the magnetic moment, and thus are likely to be paramagnetic.

One should also note that without spin polarization, some of the molecularly adsorbed oxygen configurations have positive adsorption energy. These energies become negative (exothermic) only with spin polarization turned on. Also note that on Pt(100) there is no metastable molecularly adsorbed configuration for Hv, Bx, Tv, and Tx, i.e., the energy monotonically increases as the O_2 molecule approaches the surface through these channels. For the Td channel, there is a metastable adsorption state, but with positive adsorption energy.

Finally, we comment briefly on the energy variation as the O_2 molecule approaches the surface. We consider only cases with O_2 approaching the surface vertically without rotation. Without any restriction in spin selection, we found that for the Hx and By channels, there is no energy barrier for O_2 to adsorb molecularly, except for perhaps a very small barrier for the Hx channel on Pt(100). Calculations for other channels also show generally no or a very small barrier to molecular adsorption, as long as adsorption is exothermic.

B. O_2 dissociation on a clean surface

In this section, we focus on one-dimensional (1D) energy pathways for O_2 dissociation, where we restrict motion of the dimer so that the constituent atoms separate along one fixed direction when projected onto the surface x-y plane. Here, we fix the x and y coordinates of the two oxygen atoms at various separations, and relax their z coordinates. We relax the positions of all substrate atoms except the bottom substrate layer which is fixed at the bulk geometry. In general, such 1D cuts of a high-dimensional potential energy surface provides limited information, and will not correctly identify the transition states (TSs) for dissociative adsorption. The energy at an apparent TS in the 1D cut is generally above that of the true TS. However, for specific high-symmetry pathways, selection of reaction coordinates accounting for the surface symmetry and for the known final stable adsorption sites can enhance the utility of our 1D cuts in reflecting the energetics of dissociation. For example, the Hx pathway on a clean surface unambiguously leads to separation of O atoms along the [011] direction to the most stable NN vicinal br sites for Pt and Ir, and further separation to the most stable third-NN (3NN) 4fh sites for Pd, Rh, or Ni. On the other hand, 1D cuts for the Hx pathway on a partially covered surface will not generally reflect the correct TS. Nonetheless, even in the latter situation, comparison of the behavior of 1D cuts for different surfaces may reasonably reflect the actual trends in TS behavior.

Figure 2(a) shows a series of 1D cuts of the PES for *O_2 dissociation on Pd(100)*. In the panel labeled by H, the center of the dimer is fixed at a 4fh site. For panel B, the center is fixed at a bridge site, and for panel T, the center is fixed at a top site. For panels H and T, the dimer is stretched either along the [011] close-packed direction, or diagonally. For panel B, the dimer is always stretched along a [011] close-packed direction, but towards either two NN 4fh sites or two NN top sites. The x axis of all plots is the distance $\tilde{d}$ between the two oxygen atom projected to the (100) substrate plane, so that $\tilde{d} = d$, the actual distance between the two oxygen atoms for a molecule parallel to the surface. For completeness, we also extend the 1D cut to shorter projected separations where the molecule will tilt

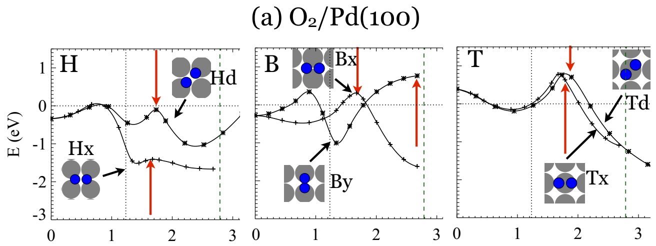
(a) O_2/Pd(100)

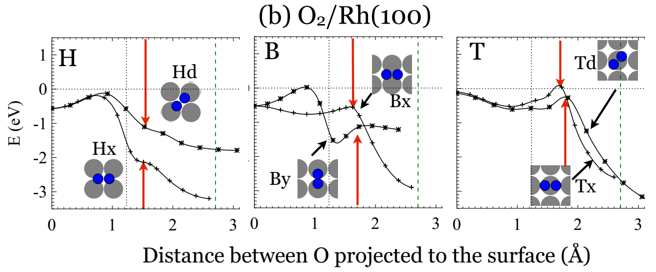
(b) O_2/Rh(100)

FIG. 2. (Color online) 1D cuts of O_2 dissociation PES on: (a) Pd(100); (b) Rh(100). These show the adsorption energy (per dimer) of as a function of the distance between the two oxygen atoms projected onto the surface plane. The center of the dimer is fixed at a 4fh site (H), a bridge site (B), and a top site (T), respectively. The vertical dot-dashed line represents the distance between the two atoms in an O_2 molecule in vacuum. The green dashed lines correspond to the surface lattice constant a, i.e., distance between NN sites, and the red arrows indicate transition states (TSs), and in cases where TSs do not exist, inflection points in 1D PES cuts.

away from the surface plane, e.g., $\tilde{d} = 0$ corresponding to a vertical O_2 molecule.

For Pd(100), the most facile pathway is the one labeled Hx. Starting from a flat-lying molecularly adsorbed O_2 centered at a 4fh site, only a small energy barrier must be overcome for the dimer to dissociate. The energy of the (symmetry-constrained) TS is 1.4 eV below that of a spin-polarized O_2 dimer in vacuum (defined as zero), and it is only slightly higher (0.12 eV) than the most stable nondissociated adsorbed state. Thus, effectively this dissociation pathway is nonactivated since the barrier is surmounted nonthermally if only a small fraction of energy gained by the molecular adsorption of O_2 is transferred to the internal stretching of the dimer.

A less facile pathway is in the same panel labeled Hd, with the two O atoms stretching diagonally. Here, the symmetry-constrained TS energy is much closer to zero, and rotation in the surface plane towards a [110] direction would lead to more facile dissociation. All other pathways for dissociation have symmetry-constrained TS energies above zero. For example, although By is a favorable molecular adsorption configuration, there is a strong energy barrier for dissociation with oxygen atoms going over two NN top sites, and rotation in the surface plane will not remove the barrier. If the center of the molecule is not constrained above the br site, it will shift towards the 4fh site, allowing dissociation through a more favorable pathway such as Hx. Our results confirming the preference of Hx over By are consistent with previous DFT studies for these two pathways [23].

For the above two pathways and others, we often find a symmetry-constrained TS for the transition from molecular physisorption to dissociated chemisorption for a projected separation of about 1.7–1.9 Å. (An exception is for By when the PES increases strongly for larger separations.) Below, we will identify a pseudo-TS for similar projected separations on Rh and other metals, even in cases where adsorption is not activated so this pseudo-TS is just reflected in a weak inflection point (but not a local maximum) in the PES. This identification will be useful for our subsequent discussion and treatment of the effect of preadsorbed O on dissociation of oxygen. The above results are obtained from DFT calculations of (2 × 2) supercells with three-layer slabs. Because of the relatively small supercell, results for larger separations (beyond 3 Å) are affected by intercell adspecies interactions and are not reliable.

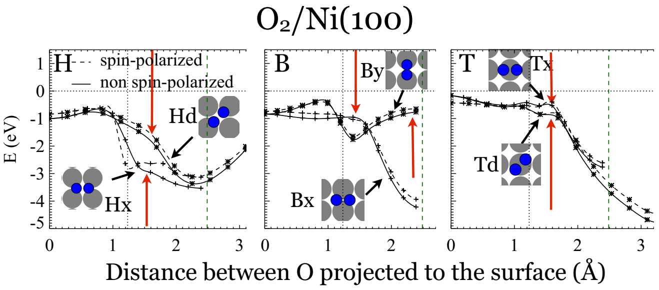

FIG. 3. (Color online) As Fig. 2, but for O_2 dissociation on Ni(100). The solid lines are obtained from non-spin-polarized DFT, and the dotted lines are obtained from spin-polarized DFT calculations. Note that the surface lattice constant a for Ni of 2.49 Å is significantly smaller than for Pd, Rh, Pt, or Ir.

Figure 2(b) shows analogous 1D PES cuts for *O_2 dissociation on Rh(100)*. These cuts are qualitatively similar to those for Pd(100), but generally reflect stronger binding of oxygen to the Rh surface compared to the Pd surface. Correspondingly, more pathways for dissociation are nonactivated with pseudo-TS energy lower than zero (where these pseudo-TSs often have a projected separation of around 1.7–1.9 Å).

Figure 3 shows similar PES plots for *O_2 dissociation on Ni(100)*. For other metals, only non-spin-polarized calculations are reported (Fig. 2 for Pd and Rh, and Fig. 4 for Pt

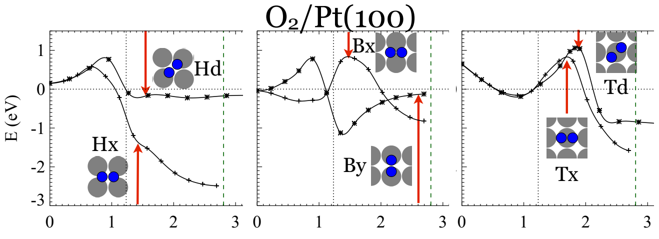
O_2/Pt(100)

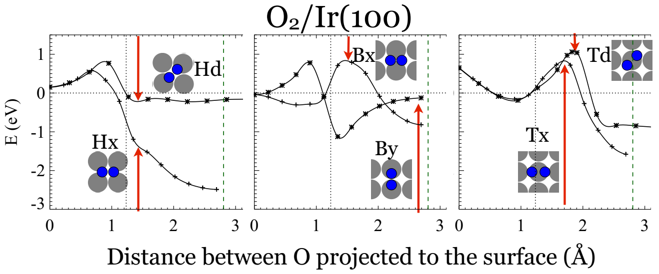
O_2/Ir(100)

FIG. 4. (Color online) As Fig. 2, but for the O_2 dissociation PES on Pt(100) and Ir(100).

and Ir), since limited tests with spin-polarized calculations show relatively small differences as long as the oxygen atoms are fairly close to the surface. For Ni(100), both spin-polarized and non-spin-polarized results are shown, noting the ferromagnetism of bulk Ni. The shapes and the energy values of the PES are very similar to those for O_2/Rh(100). One caveat is that the smaller surface lattice constant, a, of 2.49 Å for Ni means that the pseudo-TSs are generally located at smaller projected separations of around 1.5–1.7 Å (the same fraction of a lattice constant a as for Rh, etc.).

Figure 4 shows the 1D PES cuts for *O_2 dissociation on Pt(100) and Ir(100)*. Although the bridge site is the preferred adsorption site for these two systems, in contrast to the hollow site for Pd, Rh, and Ni, the PES cuts still appear qualitatively similar to those above. Here again we show six symmetric pathways with the center of the O_2 dimer fixed above the high-symmetry adsorption site. Note that for the Td pathway for Pt(100), the substrate is frozen, in contrast to all other studies, due to the large amount of substrate relaxation. Figure 4 suggests that dissociation of O_2 on unreconstructed Pt(100) and Ir(100) is quite similar. The main difference is that the overall binding of oxygen to Ir(100) is much stronger. The Hx pathway, with the final configurations of two oxygen atoms occupying a pair of vicinal NN bridge sites, is the most facile. As for Rh(100), the molecular adsorption configuration Hx is unstable to dissociation for Pt(100) and Ir(100), suggesting that the Hx pathway for dissociation should be particularly facile.

C. O_2 Dissociation on $p(2 \times 2)$-O and other oxygen adlayers

The sticking coefficient of *O_2 adsorption on Pd(100)* is reported to exhibit a precipitous drop at an oxygen coverage of around 0.25 ML, where the oxygen adlayer exhibits $p(2 \times 2)$ ordering [4,6,7]. In marked contrast, sticking on $p(2 \times 2)$-O adlayers on Rh(100) is still substantial [36]. To elucidate this contrasting behavior, and more generally to assess the effect of preadsorbed oxygen on the dissociative adsorption of O_2, we perform DFT calculations for adsorption on perfect $p(2 \times 2)$-O adlayers and on related adlayers using a larger $(2\sqrt{2} \times 2\sqrt{2})R45^\circ$ supercell. For Pd(100), Fig. 5 shows the 1D PES cut for the Hx pathway for the dimer stretched in the [110] direction with its center fixed above the central 4fh site. The behavior is shown for varying numbers of preadsorbed oxygen atoms at 2NN 4fh sites. The PES is raised as the number of preadsorbed oxygen atoms increases. This indicates that repulsion between oxygen adsorbates is not just limited to dissociated oxygen atoms at the bridge and 4fh adsorption sites, but also applies for molecularly adsorbed oxygen, and most significantly for the oxygen molecule in the TS. (Based on the analysis of other pathways in Sec. II B, we claim that the symmetry-constrained TS for this Hx pathway corresponds to the TS for the most facile dissociation pathway.)

Furthermore, the above results suggest that a simple pairwise-additive picture can reasonably characterize these “unconventional” interactions between O at the TS and preadsorbed O at 4fh sites. From the above results, one can estimate the strength of this pairwise repulsion from the incremental rise in the plots with increasing number of nearby O atoms as about 0.25 eV, corresponding to a lateral separation of about 3.4 Å ($\approx 1.2a$). We might also note that such unconventional interactions can be determined systematically and directly by DFT, as was done in previous realistic modeling of cooperative diffusion kinetics of metal adatoms on metal surfaces [37,38].

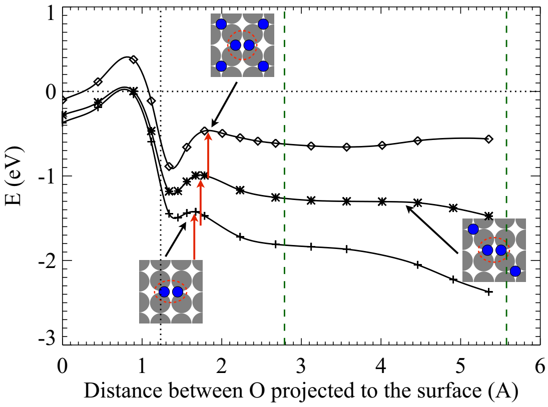

FIG. 5. (Color online) 1D cut of O_2 dissociation PES on Pd(100) for a dimer in a $(2\sqrt{2} \times 2\sqrt{2})R45^\circ$ supercell with varying number of preexisting oxygen adatoms. The lowest curve has no preadsorbed O atom, the middle curve has one preadsorbed O atom, and the top curve has two preadsorbed O atoms, forming a $p(2 \times 2)$ ordering.

Within a pairwise-interaction picture, one can go further to elucidate some aspects of the form of these PESs as the projected separation increase from around a to $2a$ for Pd(100). The energy change reflects the enhanced bonding to hollow versus bridge sites, as well as the change in lateral repulsive interaction energy. The latter corresponds to the difference between (i) a NN br site self-repulsion between O atoms in the dissociating molecule plus $(\sqrt{5}/2)a$ repulsion with preadsorbed O in the initial state, and (ii) the stronger nearest-neighbor hollow site repulsion in the final state. These changes roughly cancel each other for a $p(2 \times 2)$-O adlayer to produce a fairly flat PES. See Appendix A for a listing of “conventional” lateral interactions with both adspecies at adsorption sites.

To summarize, from Fig. 5, the energy of a dissociated state on the clean surface is lower than that of the molecularly adsorbed state. For the adlayer with $1/8$ ML O coverage, the energies in the dissociated and molecularly adsorbed states are almost equal. For a $p(2 \times 2)$ O adlayer with $1/4$ ML coverage, a molecularly adsorbed configuration has the lower energy, and the dissociation process is endothermic. Thus, the presence of preexisting O adsorbates inhibits dissociation of O_2 on a Pd(100) surface.

However, our DFT analysis indicates that molecularly adsorbed oxygen on a $p(2 \times 2)$ O adlayer on Pd(100) would almost certainly adsorb dissociatively rather than desorb (as the latter requires overcoming a substantially larger barrier). The constituent O adatoms could then diffuse almost barrier-free out of the $p(2 \times 2)$ unit cell into which they adsorbed to strongly bound 4fh sites with no neighboring O in the adjacent cells. Thus, this picture would imply significant sticking on a $p(2 \times 2)$-O adlayer, contrasting the results of experiment [4,6]. We expect that the source of this inconsistency lies in the inability of DFT to estimate the value of the TS energy relative

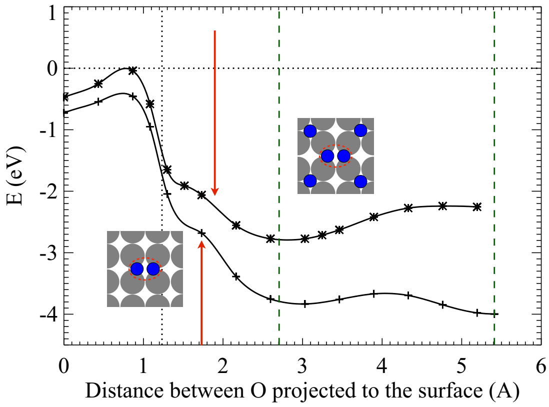

FIG. 6. (Color online) 1D cut of O_2 dissociation PES on Rh(100) for a dimer on a clean surface (lower curve) and with a preexisting $p(2 \times 2)$ O, using a $(2\sqrt{2} \times 2\sqrt{2})R45^\circ$ supercell and three-layer slab.

to the gas phase, and that the actual TS energy is higher than (rather than lower than) the latter. This deficiency will be corrected in an *ad hoc* fashion in our statistical mechanical modeling below.

For *O_2 adsorption on Rh(100)*, Fig. 6 indicates that the effect of preadsorbed O is similar to that presented above for Pd(100) in Fig. 5. While the overall shape of the PES is quite different from that for O on Pd(100), the difference between the two curves for the clean and $p(2 \times 2)$-O covered surfaces is similar for both metals. This suggests a similar picture of direct quasipairwise unconventional interactions in raising the TS energy for the precovered surface. As for Pd, the form of these PESs as the projected separation increases from around a to $2a$ can be elucidated in terms of changes in adsorption and conventional interaction energies. The significant increase for the $p(2 \times 2)$-O case [cf. Pd(100)] reflects particularly strong nearest-neighbor repulsions for hollow sites on Rh(100).

Comparing behavior for Rh(100) and Pd(100), first the 1D PESs for Rh(100) are generally much lower for Rh(100) than for Pd(100). Even with the type of *ad hoc* correction mentioned below, the TS energy remains below the gas phase energy even for a $p(2 \times 2)$-O covered surface. Second, on Pd(100), there is a small energy barrier for a flat-lying molecular adsorbed O_2 to dissociate, and the barrier increases due to repulsion with preexisting O. In contrast, there is no barrier of O_2 dissociation on Rh(100), even with a preexisting $p(2 \times 2)$ oxygen layer. These observations suggest more facile dissociation on a $p(2 \times 2)$-O adlayer on Rh(100) consistent with experiment.

For a brief discussion and analysis of adsorption pathways in lower-symmetry adlayer environments, we refer the reader to Appendix B.

III. STATISTICAL MECHANICAL MODELING OF O_2 DISSOCIATION KINETICS

A. Realistic multisite lattice-gas modeling

Our DFT analysis does not support the Brundle-Behm-Barker eight-site model [2] with selection of 2NN 4fh adsorption sites subject to a blocking constraint. Instead a variety of adsorption pathways may exist, generally favoring NN adsorption sites. Our goal is to map the real continuous-space dissociative adsorption process for oxygen onto a discrete multisite lattice-gas (MSLG) framework suitable for statistical mechanical modeling. To this end, we recall that for different possible impingement points with the center of the oxygen molecule above (a) 4fh; (b) top; and (c) br sites (of which there are two per unit cell), one anticipates dissociative adsorption to (a) NN vicinal br sites (separated by a 4fh site); (b) NN geminal br sites (the latter being separated by a top site), and perhaps to 2NN 4fh sites; and (c) NN 4fh sites or NN top sites, respectively. In the absence of steering, these impingement points are most naturally chosen with probabilities (a) 1/4, (b) 1/4, and (c) 1/2, respectively. Then, it remains to specify the relative weights for selection of the different possible pairs of sites for (b) and (c). The default choice below excludes selection of 2NN 4fh sites for (b), and chooses NN 4fh and NN top with equal probability for (c).

This yields our *canonical MSLG model for oxygen adsorption* in which just NN vicinal br (Hx), geminal br (Tx), 4fh (Bx), and top sites (By) are selected with equal probabilities as adsorption sites for oxygen. This choice is applied for all surfaces $M =$ Pd, Rh, Pt, and Ir. However, the degree of activated adsorption will depend on the metal M and also on the adsorption pathway (Hx, Bx, Tx, or By).

The activation barrier for dissociation is assumed to have the generic form

$$E_{\mathrm{act}} = E_{\mathrm{ads}} + \Delta E_{\mathrm{TS}}, \qquad (1)$$

where E_{ads} is the adsorption energy of a dissociated dimer occupying the NN sites, and ΔE_{TS} is an extra energy barrier for the transition state. An operating assumption in this paper is that ΔE_{TS} is independent of the local arrangement of adspecies (but it does depend on the dissociation pathway). This assumption can be rationalized by the observation that the lateral separation between the two oxygen atoms in the TS is just below 2.0 Å, while the separation between two oxygen atoms occupying NN adsorption sites is not much larger at about 2.5–2.8 Å. Therefore, the change of energy due to lateral interactions with preexisting adsorbates from the transition state to the "final" NN adsorption state is small. Most of the energy change is due to local interactions with the substrate which is captured by ΔE_{TS}.

Table II gives DFT values for ΔE_{TS} for various metals for each of the Hx, Bx, and Tx pathways. These values are reasonably robust for a given pathway, at least for Bx and

TABLE II. DFT values (in eV) of ΔE_{TS} for the Hx, Bx, and Tx adsorption pathways on a clean surface. We also obtain values for Hx of 0.02 (0.8) eV for a $p(2 \times 2)$-O adlayer on Pd (Rh). Results are obtained assuming that at the pseudo-TS the dimer separation is $0.56a$, and averaging over slab thickness from three to five layers in (2×2) supercells.

M	Pd	Rh	Ni	Pt	Ir
Hx	0.3	1.3	0.8	1.0	1.8
Bx	1.9	2.5	2.9	1.6	2.3
Tx	1.7	2.6	2.1	2.3	3.0

Tx which have higher ΔE_{TS} values. However, as noted in the previous section, there are limitations in the reliability of DFT analysis for the TS energies. Thus, instead of using DFT results directly, here we adopt *ad hoc* values for ΔE_{TS}. The simplest "minimal" model would just select a single value of ΔE_{TS} for all dissociation pathways. However, our DFT PESs indicate large differences in ΔE_{TS} for different pathways, e.g., ΔE_{TS} for the Hx pathway is well below that for Bx or Tx. Thus, we will focus on analysis of a "refined" model, selecting 1.0 eV for Hx, 3.0 eV for Bx, and Tx, and 0.0 eV for By. (For comparison, we do present limited results for a minimal model with all $\Delta E_{TS} = 1.0$ eV.)

A complete prescription of a realistic adsorption model also requires an appropriate description of the oxygen adlayer structure and diffusive dynamics. In our analysis, this is based on DFT values for site-specific adsorption energies and pairwise adspecies interactions listed in Appendix A. Diffusion is implemented allowing both "short" hops of distance $a/2$ between br-4fh and br-top pairs, and of distance $a/\sqrt{2}$ between br-br and 4fh-top pairs, and "long" hops of distance a between sites of the same type. Barriers are selected according to METROPOLIS dynamics and satisfy a detailed-balance condition consistent with the adspecies adsorption and interaction energies. In the following sections, we present kinetic Monte Carlo (KMC) simulation results for the minimal and refined models for the coverage and temperature dependence of sticking. We refer the reader to the Appendix C for a description of the KMC algorithm, including a detailed discussion of the choice of prefactors for hopping.

For our MSLG adsorption model prescribed above, it is instructive to anticipate and enumerate a variety of dissociative adsorption events which may occur in simulation studies of the coverage dependence of sticking. For Pd, Rh, and Ni, apart from the preference for 4fh adsorption sites, these adsorption events will reflect the feature that interaction energetics strongly disfavor NN 4fh O. Adsorption via the predominant Hx pathway creates disfavored NN vicinal br O, and as a result thermal hopping should quickly eliminate these configurations, with the O adatoms further separating to preferred 4fh sites, while at the same time avoiding the formation of NN 4fh pairs. Figure 7(a) illustrates a variety of such events where limited diffusive motion readily avoids NN 4fh O in the final configuration. However, for higher coverages, this becomes more difficult and the overall adsorption process has nonlocal aspects. By this we mean that the adsorption process depends on the adlayer configuration in a larger region around the impingement sites, and that preadsorbed species may also be required to rearrange in order to avoid creation of disfavored configurations.

For Pt and Ir, oxygen adsorption events will reflect a preference for the br adsorption sites, and also the feature that interactions favor vicinal and disfavor geminal NN br O. For adsorption via the predominant Hx pathway on Pt and Ir, the resulting NN vicinal br pair of O atoms are energetically favored on a clean surface, so that no subsequent hopping is required to remove unfavorable configurations for a clean surface. However, the presence of nearby preadsorbed O can require hopping to avoid formation of NN geminal br pairs. See Fig. 7(b).

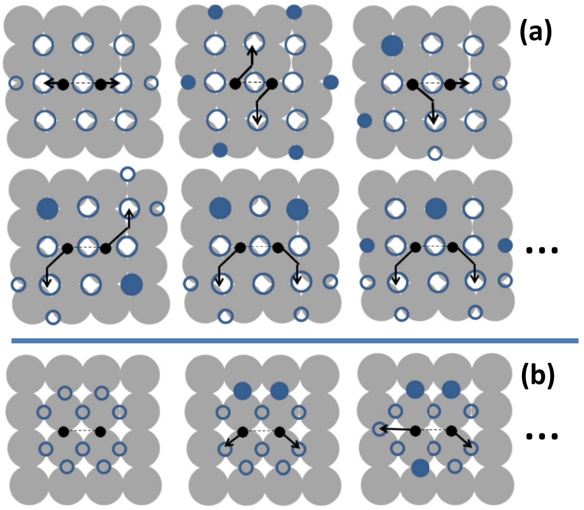

FIG. 7. (Color online) Dissociative adsorption and subsequent thermal hopping pathways with Hx impingement for various local adlayer configurations. (a) Examples with preferred 4fh adsorption sites where hopping removes energetically costly NN 4fh O. (b) Examples with preferred br adsorption sites where hopping removes energetically costly geminal NN br O. Black filled circles denote the O atoms in the impinging molecule, and arrows denote thermal hopping paths; open (filled) blue circles denote sites free of (populated by) preadsorbed O.

Below, we focus on simulation results for the normalized sticking coefficient

$$\hat{S}(\theta_O) \equiv S(\theta_O)/S(0) \approx 1 - c_1\theta_O + c_2(\theta_O)^2 + \cdots, \qquad (2)$$

for low θ_O. The results for c_1 obtained from a linear fit of data between 0 and 0.1 ML are provided in Table III for both the minimal and refined models for $M =$ Pd, Rh, Pt, and Ir. Our simulations are performed with an oxygen adsorption rate of $P_{O_2} = 1$ ML/s on the clean surface at various T, and the sticking coefficient is determined from the slope of the oxygen uptake curve.

B. Simulation results for oxygen on M(100) with $M =$ Pd, Rh, Ni, Pt, and Ir

1. Pd(100)

In the minimal model with $\Delta E_{TS} = 1.0$ eV for all pathways, three dissociation pathways are nonactivated, i.e., Hx, Bx, and

TABLE III. The number of nonactivated dissociation pathways N_p and c_1 values where $S(\theta_O) \approx 1 - c_1\theta_O$. Results are obtained from simulations of 2048^2-site systems with capping rate of $\upsilon_l = 100\ \mathrm{s}^{-1}$ at 300 K. Results are reported for the minimal model with $\Delta E_{TS} = 1.0$ eV for all dissociation pathways, and for the refined model with different ΔE_{TS} for different pathways.

		Pd(100)	Rh(100)	Pt(100)	Ir(100)
Minimal	N_p	3	4	3	4
	c_1	3.19	3.51	4.00	3.09
Refined	N_p	1	4	2	3
	c_1	3.49	4.25	4.02	3.49

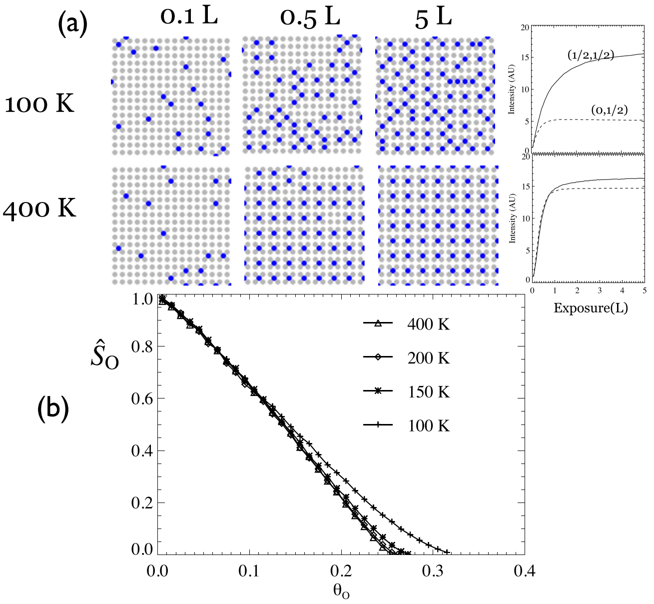

FIG. 8. (Color online) (a) Real-space configuration of oxygen (blue dots) from KMC simulation of O_2 adsorption on Pd(100) surface (refined MSLG model). Also intensities I of (1/2,1/2) (solid) and (1/2,0) (dashed) diffraction spots. (b) Normalized sticking coefficient versus coverage.

Tx on a clean surface. In the refined model with multiple ΔE_{TS} values, only one pathway, Hx, is nonactivated on a clean surface. The latter is more consistent with the DFT results in Sec. II B. Simulations show a quasilinear decrease of the normalized sticking coefficient at least up to 0.1 ML, behavior which is almost independent of temperature. This allows unambiguous determination of $c_1 = 3.19$ (3.49) in the minimal (refined) model.

Simulations show that for T above about 150 K, adsorbed oxygen has sufficient thermal mobility for the adlayer to achieve good $p(2 \times 2)$ ordering at around 0.25 ML. See Fig. 8(a) (bottom frame). Thus, based on the analysis of Sec. II (specifically Fig. 5) and accounting for our *ad hoc* form of E_{act}, dissociative adsorption is activated in this case, and is strongly inhibited at around 0.25 ML resulting in a very low S above this coverage. This results in an effective saturation coverage θ_O^S of around 0.25–0.26 ML. For T below 150 K, there is insufficient thermal diffusion for oxygen to form large well-ordered $p(2 \times 2)$ domains, so that significant O_2 dissociation can still occur along domain boundaries. See Fig. 8(a) (top frame). Consequently S remains substantial at 0.25 ML, and becomes small only at an effective θ_O^S somewhat above 0.3 ML. At 150 K, θ_O^S around 0.27–0.28 ML is just above that at higher T values. The behavior of S is illustrated in Fig. 8(b).

One caveat is that the above estimates of θ_O^S were obtained from simulations with an exposure of around 5 langmuir (L). For higher T of 400 K or above, prolonged exposure (for tens of L) can lead to oxygen coverages significantly above the nominal saturation value of around 0.25 ML. We note that reducing ΔE_{TS} for Hx somewhat below 1.0 eV can also increase θ_O^S. The same applies to reducing the strength of the repulsion between O adatoms at 2NN 4fh sites below the DFT value of 0.13 eV (see also Ref. [39]), a change which may actually enhance agreement with the experimental phase diagram for O ordering on Pd(100) [16].

The occurrence of saturation coverages θ_O^S around 0.3 ML is consistent with experimental analysis in the regime of lower temperatures [4,6]. Consideration of this regime avoids any complications due to surface reconstruction which is not included in our modeling [6,40]. Figure 8(a) shows the (1/2,1/2) and (0,1/2) diffraction spot intensities for different exposures obtained from simulation results. The feature of an intense (1/2,1/2) spot and weaker (1/2,0) spot at lower T, versus similar intensities at higher T, is also entirely consistent with experimental low-energy electron diffraction data [4,5]. It should be emphasized that our MSLG model is quite different from the eight-site model used previously to obtain this behavior.

2. *Rh(100)*

For Rh(100), both the minimal and refined models allow four nonactivated dissociation pathways for the clean surface. We find that $c_1 = 3.50$ (4.25) in the minimal (refined) model. Unlike for Pd(100), the sticking coefficient is still significant at 0.25 ML. Also, there is minimal temperature dependence of the sticking coefficient even down to 100 K. This feature indicates that ordering does not have as significant an influence for O_2 adsorption on Rh(100), contrasting the behavior for Pd(100). Figure 9(a) reveals less perfect ordering than for Pd(100) at higher T. For the minimal model, the normalized sticking coefficient drops below 0.1 for $\theta_O > 0.33$ ML, and drops below 0.01 for $\theta_O > 0.45$ ML. For the refined model, $\hat{S}(\theta_O)$ reaches these two thresholds slightly earlier, at 0.325 and 0.43 ML, respectively. This behavior for S is illustrated in Fig. 9(b). This slower decrease compared to Pd is quite consistent with experimental assessment of O_2 sticking using the method of King and Wells [9]. The latter suggests a smaller c_1 value than the above estimates (likely below 2). This could

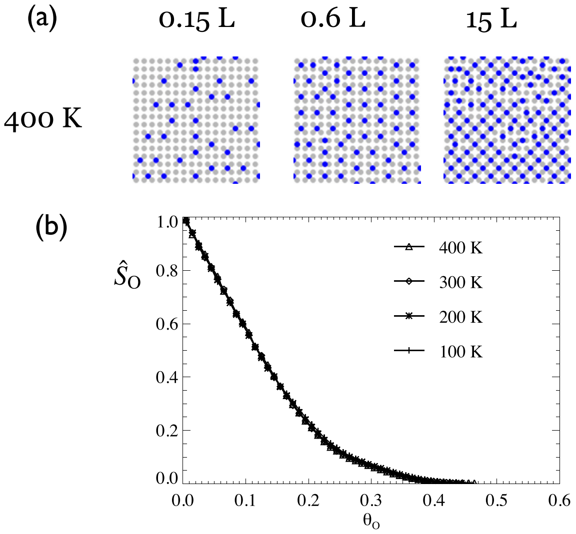

FIG. 9. (Color online) (a) Real-space configuration of oxygen (blue dots) from KMC simulations of O_2 adsorption on Rh(100) surface (refined MSLG model). (b) Normalized sticking coefficient versus coverage.

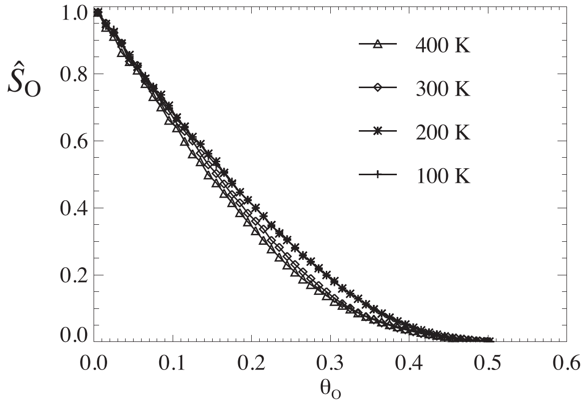

FIG. 10. Normalized sticking coefficient from KMC simulations of O_2 dissociation on Ni(100) (refined MSLG model).

be due to the effect of molecular precursors, or due to the effects of steering and funneling dynamics [20] not included in our modeling. See also Sec. IV.

3. *Ni(100)*

The sticking behavior for oxygen dissociation on Ni(100) using the refined model is very similar to the case of Rh(100). See Fig. 10. As for Rh(100), substantial sticking still occurs when oxygen coverage is 0.25 ML, and sticking remains active up to around 0.4 ML. These results appear fundamentally inconsistent with the early experimental studies of Holloway and Hudson [1] and Brundle *et al.* [2] which prompted development of the eight-site model. We recall that this model implies saturation at 0.25 ML for $p(2 \times 2)$-O adlayers. However, a later study by Stuckless *et al.* [3] argued that both earlier studies suffered from coverage miscalibration due to the assumption of an initial sticking coefficient of unity. Using a lower value of 0.63 to recalibrate the coverage led to an increased saturation coverage close to the estimate by Stuckless *et al.* of 0.38 ML. This behavior is consistent with our MSLG modeling.

4. *Pt(100) and Ir(100)*

For Pt(100), the minimal model predicts three nonactivated pathways Hx, Tx, and By for dissociative adsorption of oxygen on the clean surface. The refined model predicts two pathways Hx and By. The behavior of the normalized sticking coefficients of the two models are quite similar, both having c_1 around 4.0. The saturation coverage is sensitive to the choice of interaction energetics in this system. We find that using a set of adspecies interaction parameters determined previously to capture behavior for low to medium coverages (<0.5 ML) [20], the saturation coverage is quite high, above 0.6 ML, compared to experimental estimates [10]. This prompts us to consider more carefully the selection of interactions to capture the behavior at higher O coverage. Using as input a set of ten configurations with oxygen occupying bridge sites, we derive a set of seven pairwise interactions using least-squares regression. Simulations using this set of parameters produce a saturation coverage of 0.5 ML, consistent with experiment [10]. For this choice of interaction parameters, real-space adlayer configurations at 400 K are shown in Fig. 11(a) and the sticking coefficient versus coverage is reported in Fig. 11(b). One caveat is that giving more weight to describing higher coverage configurations may lead to a poorer description of adlayer ordering for various lower coverage configurations. Any such shortcomings likely reflect limitations in the use of pairwise interactions in the current MSLG modeling.

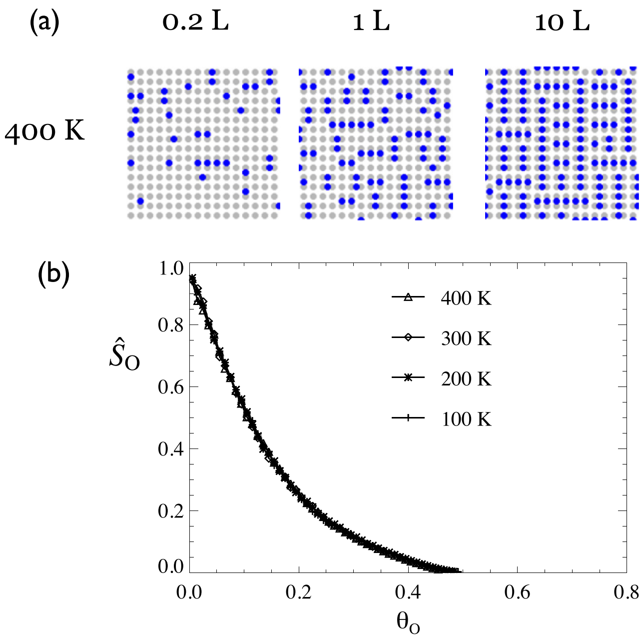

FIG. 11. (Color online) (a) Real-space configuration of oxygen (blue dots) from KMC simulations of O_2 adsorption on Pt(100) surface (refined MSLG model). (b) Normalized sticking coefficient versus coverage.

For our model using $\Delta E_{TS} = 1.0$ eV, the activation barrier for adsorption between (2×1) O rows via the Hx pathway is very close to zero. Whether the actual value is above or below zero depends on the procedure through which one selects the interaction energetics (in addition to the *ad hoc* choice of ΔE_{TS}). Indeed, experiments show [10] that the sticking coefficient at 0.5 ML is very sensitive to the incident energies of the molecular beam, a feature which dovetails nicely with the picture that the TS energy for dissociation between rows is close to zero.

For Ir(100), the minimal model predicts four nonactivated pathways for dissociative adsorption of oxygen, while the more refined model predicts three (Bx is now activated). The saturation coverage of around 0.8 ML for 150 K or above is significantly higher than that for Pt(100). This reflects the stronger binding of oxygen to Ir(100). For low T of around 100 K, the saturation coverage is lower as the adlayer cannot as readily expel domain boundaries between degenerate (1×1)-O domains. Real-space adlayer configurations are shown in Fig. 12(a) and the sticking coefficient versus coverage is reported in Fig. 12(b). We also note that adspecies interaction energies derived from DFT for Ir(100) are not as sensitive to the fitting procedure as for Pt(100).

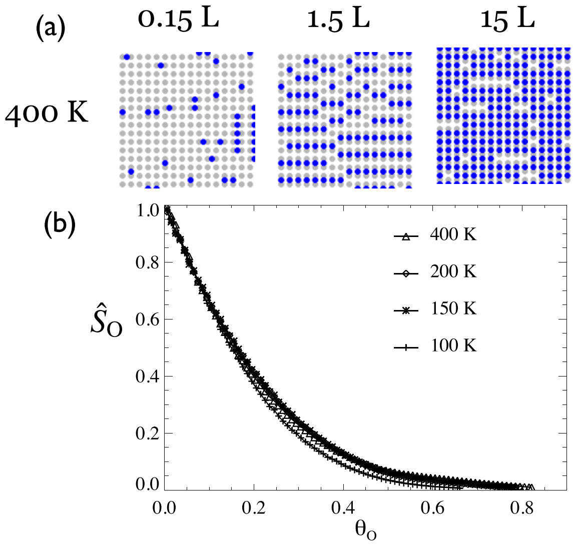

FIG. 12. (Color online) (a) Real-space configuration of oxygen (blue dots) from KMC simulations of O_2 adsorption on Ir(100) surface (refined MSLG model). (b) Normalized sticking coefficient versus coverage.

IV. SIMPLE SINGLE-SITE ADSORPTION MODELS

A. Random sequential adsorption–type models for preferred 4fh sites (Pd, Rh, and Ni)

The eight-site model has considerable value providing a simple and general adsorption rule which can be incorporated into statistical mechanical modeling of the coverage dependence of sticking. Significantly, it is applicable for both higher T with quasiequilibrated adlayers, and also for low T where limited thermal mobility results in far-from-equilibrium adlayer ordering. Since oxygen adlayers do *not* have significant population of NN 4fh sites even at low T, it is particularly appealing that the eight-site model automatically enforces this feature even in the complete absence of thermal mobility. In this zero-mobility regime, the model falls within a class of so-called random sequential adsorption (RSA) models which exhibit nontrivial nonequilibrium jammed or saturation states [15,41]. The jamming coverage for the eight-site RSA model is $\theta_O^J = 0.362$ ML, and a near-jammed adlayer configuration is shown in Fig. 13(a). However, there is clear indication from DFT analysis that adsorption does not occur on 2NN 4fh sites as in the eight-site model. This prompted consideration in the previous section of more realistic but complex MSLG models.

Here, our focus is on the development of simple alternatives to the eight-site model which better mimic behavior in the refined MSLG model for Pd(100), where a single adsorption pathway, Hx, dominates, and where adsorbed O reside exclusively at 4fh sites. While this pathway initially produces dissociated O on neighboring vicinal bridge sites, these quickly separate to non-NN 4fh sites due to rapid thermal diffusion, as discussed in Sec. III A. To ensure that our adsorption model captures this feature, we insist not just that the 4fh site above which is the center of the oxygen molecule adsorbs is empty, but also hollow sites on opposite sides (forming a linear triple) are empty. Our simple adsorption model then identifies the final location of the O as these third nearest-neighbor hollow sites at opposite ends of this triple. In addition, to avoid creating neighboring 4fh O, we demand that the additional six hollow sites adjacent to the final 3NN sites are empty, for a total of nine empty sites (nine-site model). Alternatively, we can demand that two extra neighboring sites adjacent to the central site of the linear triple are also empty, for a total of eleven sites (eleven-site model). See Figs. 13(b) and 13(c).

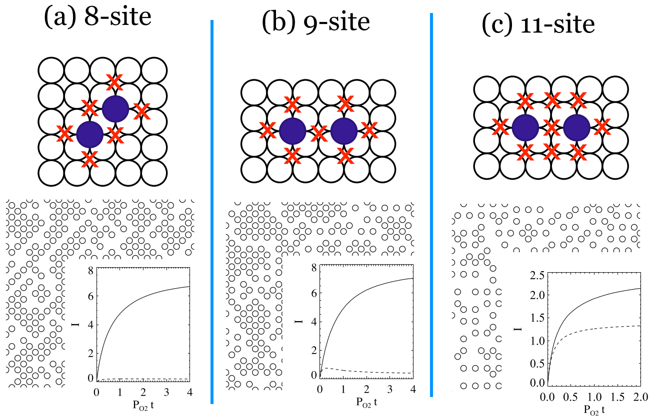

FIG. 13. (Color online) Illustration of different RSA-type models for dimer filling. Configurations near jamming in the absence of any surface mobility are shown for each model below. Also intensities I of (1/2,1/2) (solid) and (1/2,0) (dashed) diffraction spots.

The behavior of these nine-site and eleven-site RSA models in the absence of thermal diffusion is similar to that of the classiceight-site RSA model. All generate configurations with local $c(2\times2)$ ordering, and have well-defined but nontrivial jamming coverages θ_O^J in the absence of surface mobility. Specifically, one finds that $\theta_O^J = 0.361$ (nine sites) and $\theta_O^J = 0.225$ (eleven sites) ML, versus $\theta_O^J = 0.362$ (eight sites). Figures 13(b) and 13(c) show near-jammed adlayer configurations for the nine- and eleven-site models.

Of particular relevance is the feature that for these RSA models, one can readily obtain an exact Taylor expansion for the sticking coefficient in terms of coverage. Development of this expansion utilizes the exact hierarchical master equations for these nonequilibrium statistical mechanical models [15,41]. These can be compared against the behavior for low-coverage high-mobility random adlayers. For the eight-site model, c_1 equals 6 (8) for zero-mobility RSA (an equilibrated adlayer). Likewise, c_1 equals 7.25 (9) for the nine-site model, and 9 (11) for the eleven-site model for RSA (an equilibrated adlayer). The lower RSA values for no mobility reflect the enhanced nonequilibrium short-range $c(2\times2)$ ordering which boosts the population of adsorption ensembles. However, all these values are well above those obtained from our KMC simulations of a realistic adsorption model. This feature was not appreciated in previous studies using the eight-site model.

Another appeal of the simple eight-site model was its ability to capture the key features of surface diffraction studies especially in the low-T limited-mobility regime [4]. As mentioned previously, these experiments at low T revealed an intense diffuse (1/2,1/2) spot and a much weaker (1/2,0) spot, but similar intensities for high T. Both the eight-site and the nine-site models incorporate this feature, whereas the (1/2,0) spot is somewhat more intense in the eleven-site model. However, inadequacy in describing sticking (large c_1 values) motivates consideration of refined models.

B. Other adsorption models for preferred 4fh sites

Examination of the DFT + MSLG modeling indicates that the anomalously large c_1 values in the above RSA-type models reflect too restrictive adsorption rules. For example, for Pd(100), adsorption on the 0.125 ML O overlayer in Fig. 5 is nonactivated, even though two out of the six (eight) peripheral sites in the nine-site (eleven-site) model ensemble are occupied (blocking adsorption in those models). To ameliorate this deficiency, we could stipulate that the attempted dissociative adsorption is now successful if the number of preadsorbed peripheral oxygen NN neighbors does not exceed some nonzero threshold $N_{\text{threshold}}$ (but still require the central linear triple to be empty). For $N_{\text{threshold}} = 1$, master equation analysis reveals that c_1 equals 3.75 (3) for the nine-site model, and 4 (3) for the eleven-site model for zero mobility (an equilibrated adlayer). These values are close to those for our MSLG model. However, this agreement is somewhat coincidental at least for low mobility as these reduced c_1 reflect the presence of unphysical NN 4fh O in the nonequilibrium adlayer structure. Choosing $N_{\text{threshold}} = 2$, noting that two peripheral O atoms do not block adsorption for Pd, gives c_1 of 1.75 (3), but the adlayer structure is even less physical. The value $c_1 = 3$ for equilibrated adlayers reflects the requirement of an empty linear trio of sites for any $N_{\text{threshold}} \geqslant 1$ (also a feature of the MSLG model).

The shortcomings of the above simple RSA-type models are clear from enumeration of overall dissociation plus hopping pathways in Fig. 7(a) for our realistic msLG models.

To improve on the above nine- and eleven-site threshold models, we note that for the Hx pathway on Pd(100), the TS energetics is impacted only by the occupancy of linear triples immediately adjacent to a central triple of unoccupied sites above which the molecule impinges. Thus, we consider a refined 9*-site model focusing the 3 × 3 sites in these three triples, and again allow adsorption if the occupancy of the six peripheral sites does not exceed a threshold $N_{\text{threshold}}$. See Fig. 14(a). However, we now also include immediate postdeposition hopping (if needed) to avoid population of NN 4fh O pairs. First, we place the adsorbing O atoms at the end sites of the central empty triple. We randomly choose one of these atoms first. If its current site is not blocked (by a NN O), it remains there. If it is blocked, then it will test all NN and 2NN 4fh sites for availability, and one is chosen randomly. In the example of Fig. 14(b), three sites are available for the first-selected left atom. Note that these include the central empty site since the other oxygen can subsequently diffuse further from the site, making it available. If no site is free, then the adsorption of oxygen atom is aborted. The other oxygen atom is then treated similarly.

For this 9*-site model with $N_{\text{threshold}} = 1$ (mimicking the realistic MSLG model) in the RSA regime with no thermal mobility of preadsorbed O, Fig. 14(c) shows the real-space configuration near jamming, for which $\theta_O^J = 0.320$ ML, as well as the intensities of the (1/2,1/2) and (1/2,0) diffraction spots. Figure 14(d) shows the coverage dependence of the sticking coefficient. For $N_{\text{threshold}} = 1$, master equation analysis reveals that c_1 equals 4 (3) for zero mobility (an equilibrated adlayer), reasonably capturing the behavior in the MSLG model. For contrast, when $N_{\text{threshold}} = 0$, c_1 equals 7.5 (9).

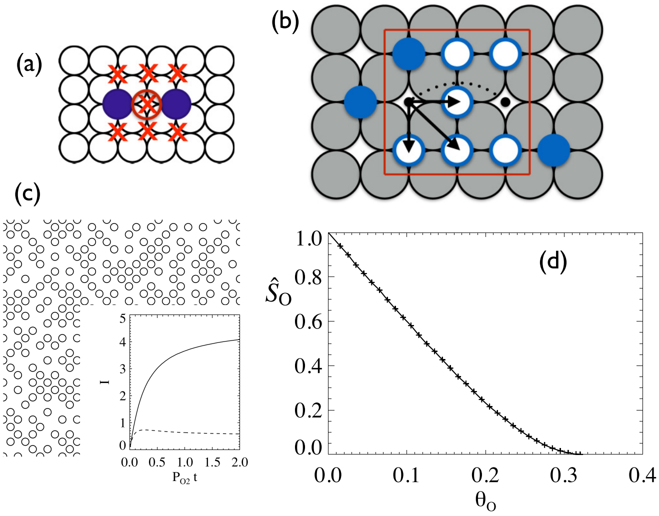

FIG. 14. (Color online) Refined 9*-site model. (a) The 3 × 3 = 9 site ensemble. The two sites with blue circles (representing O just after deposition) and the central site with the red cross must be free of oxygen. The six peripheral sites with red crosses can only have at most $N_{\text{threshold}}$ oxygen atoms. (b)–(d) are for $N_{\text{threshold}} = 1$. (b) Possible postdeposition hopping of the just deposited atoms (black dots) with only three nearby preadsorbed O atoms (blue circles). The left atom (if chosen first) can hop to one of three available sites. If it hops right, then the right atom must hop up. (c) Real-space RSA configuration near jamming, and the evolution of the intensities I of the (1/2,1/2) (solid line) and (1/2,0) (dotted line) diffraction spots. (d) Normalized sticking coefficient versus coverage for RSA.

C. RSA-type models for preferred bridge sites (Pt and Ir)

As noted previously, for O/Pt(100) and O/Ir(100), the most favorable adsorption site at low coverage is the bridge site (rather than the 4fh site). The most facile Hx dissociation pathway leads immediately to occupancy of two vicinal NN br sites. According to DFT calculations, occupation of such vicinal NN br pairs is thermodynamically favored due to an attractive NN interaction for both Pt(100) and Ir(100). This contrasts with geminal NN br pairs. Thus, in a sense, adsorption dynamics and thermodynamics work in concert in these systems.

Thus, we are motivated to consider simple RSA-type models for low-T adsorption with no thermal mobility which allow dimer dissociation only onto vicinal NN bridge sites (i.e., the Hx pathway). Two versions of RSA models are considered. In the first 8br-site model, the pair of bridge sites is available for adsorption if both sites are empty and if there is no neighboring oxygen atom within a distance $d < a$. Thus, in addition to the central pair, six additional bridge sites must be empty. See

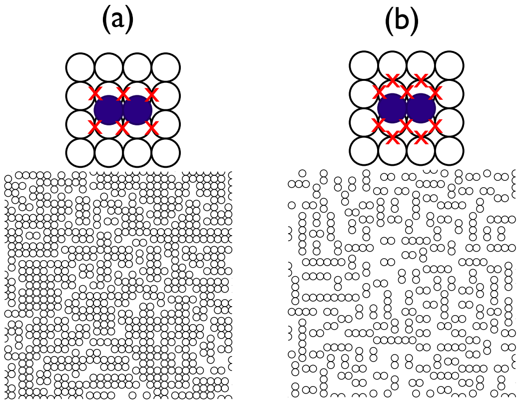

FIG. 15. (Color online) Illustration of RSA models for bridge-site oxygen adsorption. (a) 8br-site model with only vicinal NN dimer filling; (b) 12br-site model excluding any geminal NN pair. The jamming configurations for no surface diffusion are shown below the model schematics.

Figure 15(a). In the case of no surface diffusion (mimicking low T), the jamming coverage for this model is 0.706 ML, roughly twice that of the classic eight-site model (reflecting in part the ratio of br to 4fh sites). The second 12br-site model assumes that dissociation is blocked by the formation of geminal NN br pairs. So adsorption occurs only if there are no O atoms within $d < a$ of the adsorption sites, *and* no geminal NN O are formed. See Fig. 15(b). The jamming coverage of the model for no surface mobility is 0.374 ML. Finally, we mention that c_1 equals $8/2 = 4$ $(12/2 = 6)$ for the 8br-site (12br-site) model for an equilibrated adlayer, accounting for the feature that the probability that each br site is occupied equals $\theta_O/2$.

V. CONCLUSION

DFT analysis was performed to assess the energetics of O_2 dissociation on unreconstructed (100) surfaces of Pd, Rh, Ni, Ir, and Pt. Particular attention was paid to the effects of preadsorbed oxygen on the adsorption, with the intent of providing a realistic picture of sticking kinetics at low and medium coverages and for a range of surface temperatures. This was achieved by KMC simulation of a realistic msLG model that incorporates full set of adspecies adsorption energies and interactions, in addition to a realistic environment-dependent adsorption rule. The realistic but complex MSLG model was also compared with simpler RSA-type models for adsorption at lower T in the absence of significant thermal diffusion, including the previously accepted but quite distinct classic eight-site model.

As noted above, experiments show that adsorption on a 0.25 ML $p(2 \times 2)$ ordered oxygen adlayer on Pd(100) is strongly inhibited, contrasting with the DFT results in Fig. 2. This prompted *ad hoc* refinement of the activation barrier for dissociation in our MSLG modeling. The capability of DFT with the PBE uinctional to describe O_2 dissociation has been a subject of extensive debate for Al(111). There are two camps. One assumes DFT is generally accurate, but questions other underlying assumptions such as electronic adiabaticity [25]. The other questions the validity of the generalized gradient approximation to describe situations with breaking bonds [26]. Currently, the answer is not clear.

Our environment-dependent dissociative adsorption model does not capture some of the finer details of sticking behavior observed in experiments. Refinements of the current model might incorporate insights into the dependence on incident O_2 orientation of adsorption pathways in recent experiments for Pd(100) [42], more subtle steering and funneling dynamics [20], dislodging of preadsorbed adatoms during adsorption, or additional "hot-adatom" transient mobility after O_2 dissociation. The latter phenomenon has attracted attention for both metal (111) [43,44] and metal (100) surfaces [6,15,16,21,45]. Of particular note are recent hybrid *ab initio* molecular dynamics studies exploring transient mobility for oxygen dissociation on Pd(100) [21].

ACKNOWLEDGMENTS

This work was supported by the US Department of Energy (USDOE), Office of Basic Energy Sciences, Division of Chemical Sciences, Geosciences, and Biosciences through the Ames Laboratory Chemical Physics and PCTC projects. We acknowledge NERSC for providing computational resources. The work was performed at Ames Laboratory which is operated for the USDOE by Iowa State University under Contract No. DE-AC02-07CH11358.

APPENDIX A: OXYGEN ADSORPTION AND INTERACTION ENERGETICS

Table IV gives the site-specific adsorption energies and Table V gives the site-specific interaction energies for O on Pd, Rh, Pt, and Ir (100) surfaces. Results are derived from DFT calculations and averaging slab thickness from five to nine layers. Most of the interaction energetics were obtained previously from comparing two different configurations at two different coverages [20] except for br-O interactions for Pt(100), which are obtained from a new linear regression analysis (see Sec. III B 4) utilizing a set of ten configurations.

APPENDIX B: ASYMMETRIC DISSOCIATIVE ADSORPTION PATHWAYS

Our analysis above for dissociative adsorption on clean surfaces naturally considered symmetric pathways where the center of mass of the pair of oxygen atoms in the molecule remains above a high-symmetry site. The analysis above for a perfect 0.25 ML $p(2 \times 2)$ and related 0.125 ML structures

TABLE IV. Site-specific adsorption energies (in eV) incorporated into the MSLG models.

M	Pd	Rh	Pt	Ir
br	−0.940	−1.840	−1.231	−1.960
4fh	−1.220	−2.020	−0.719	−1.641
top	0.220	−0.085	−0.100	−1.184

TABLE V. Site-specific interaction energies incorporated into the MSLG model. For Pt and Ir, there are two rows for br-br interactions at $d = a$ and $d = 2a$. The first row assumes isotropic interactions, and the second row separates out the vicinal and geminal interactions.

Substrate	d/a	Top	br	4fh	Mixed
Pd(100)	1	0.142	0.219	0.368	
	$\sqrt{5}/2$				0.247
	$\sqrt{2}$	0.058	0.086	0.132	
	3/2				0.047
	$\sqrt{5/2}$	0.017	0.054	0.017	
	2		0.013	−0.036	
	$\sqrt{5}$			−0.002	
Rh(100)	1	0.148	0.238	0.464	
	$\sqrt{5}/2$				0.214
	$\sqrt{2}$	0.028	0.056	0.141	
	$\sqrt{5/2}$	0.013	0.037	0.014	
	2		0.012	−0.005	
	$\sqrt{5}/2$			0.001	
Pt(100)	1	1.045	2.08 −0.074(v), 0.373(g)	0.339	
	$\sqrt{5}/2$				0.188
	$\sqrt{2}$	−0.016	0.032	0.180	
	$\sqrt{5/2}$	0.003	0.015	0.003	
	2		0.060 0.071(v), 0.017(g)	0.003	
	$\sqrt{5}/2$		0.025		
Ir(100)	1	0.050	0.162 −0.077(v), 0.390(g)	0.378	
	$\sqrt{5}/2$				0.194
	$\sqrt{2}$	−0.008	0.010	0.124	
	$\sqrt{5/2}$	−0.002	0.044	−0.002	
	2		0.025 0.030(v), −0.020(g)	0.005	
	$\sqrt{5}/2$		−0.005		

retains significant symmetry. However, more general arrangements of adsorbates in the vicinity of the adsorption site would break any such symmetry. Thus, in general, we must characterize adsorption for such asymmetric environments which will naturally induce asymmetric dissociation pathways. One could anticipate that the PES for these pathways could be estimated by adjusting the PES for the same asymmetric pathway in the absence of adsorbates to account for the effect of pairwise conventional and unconventional repulsive interactions with nearby preadsorbed species. This motivates the analysis described below.

Figure 16 presents results for two "forced" *asymmetric dissociation pathways* for both Pd(100) and Rh(100). In both cases, one of the oxygen atoms is fixed above the 4fh site position, and the other atom is stretched along the horizontal or diagonal direction. For horizontal stretching (Ax), the molecular precursor and TS energies are higher than those of pathway Hx. Note that for the Ax pathway on Pd(100), the substrate is frozen, just as in the Td pathway for Pt(100) in Fig. 4 to avoid surface reconstruction. Dissociation via this type of pathway could be induced by a pair of preadsorbed O on second-neighbor sites to the left of the central hollow site. It is interesting that for both Pd and Rh, the Ax and Ad pathways have very similar PES curves, while the Hx and Hd pathways are quite different.

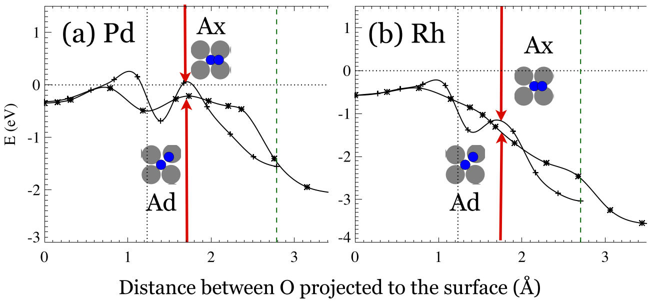

FIG. 16. (Color online) PES for asymmetric adsorption paths on Pd (a) and Rh (b).

APPENDIX C: KMC SIMULATION ALGORITHM

In the KMC code for this multisite lattice-gas model with O adatoms allowed to occupy 4fh, br, and top sites, lists of O on these different adsorption sites are maintained and updated. For each group of atoms and each type of process, we determine the maximum possible rate, e.g., hopping from 4fh to bridge sites. An upper bound $R_{\mathrm{tot}+}$ on the total rate for all processes follows from these individual maximum rates and the number of species participating in the different processes. Then, at each Monte Carlo step, time is advanced by $1/R_{\mathrm{tot}+}$, and a processes is randomly selected from the above-mentioned lists weighted by the maximum attempt rates. The probability for successful implementation of this process equals the ratio of its actual rate to the associated maximum rate. While this is not a rejection-free KMC algorithm, it can generally maintain adequate efficiency for our application at least with capping of rates for some very rapid hopping processes (which may otherwise utilize excessive computational resources). Adlayer equilibration on the time scale of adsorption is achieved above a certain threshold value for hopping, so capping rates above this threshold should not affect behavior. For low-T adsorption with unequilibrated adlayers, where some hop rates are not far above the adsorption rate, the uncapped physical values of those rates must be used. See Refs. [17,19,20] for more details.

To briefly comment further on the capping of hop rates, we note that the vibrational attempt frequency is typically taken as $\nu_0 = 10^{13}\ \mathrm{s}^{-1}$. For long hops, the attempt frequency is ideally chosen to be $\nu_l = \nu_0 \exp\left(-E_d/(k_B T)\right)$, where E_d is an estimated barrier for long-range diffusion of O across the surface. In practice, at least at higher temperatures, it may be necessary to cap the ν_l to enable more efficient simulation. For short hops, the attempt frequency is chosen to be ν_s which is capped far below.

[1] P. H. Holloway and J. B. Hudson, Surf. Sci. **43**, 123 (1974).
[2] C. R. Brundle, R. J. Behm, and J. A. Barker, J. Vac. Sci. Technol. A **2**, 1038 (1984).
[3] J. T. Stuckless, C. E. Wartnaby, N. Al-Sarraf, S. J. B. Dixon-Warren, M. Kovar, and D. A. King, J. Chem. Phys. **106**, 2012 (1997).
[4] S.-L. Chang and P. A. Thiel, Phys. Rev. Lett. **59**, 296 (1987).
[5] S.-L. Chang, D. E. Sanders, J. W. Evans, and P. A. Thiel, in *The Structure of Surfaces II*, edited by J. F. van der Veen and M. A. V. Hove (Springer-Verlag, Berlin, 1988), p. 231.
[6] S.-L. Chang and P. A. Thiel, J. Chem. Phys. **88**, 2071 (1988).
[7] G. Zheng and E. I. Altman, Surf. Sci. **504**, 253 (2002).
[8] A. Baraldi, V. R. Dhanak, G. Comelli, K. C. Prince, and R. Rosei, Phys. Rev. B **53**, 4073 (1996).
[9] R. Kose, W. A. Brown, and D. A. King, Surf. Sci. **402–404**, 856 (1998).
[10] J. M. Bradley, X.-C. Guo, A. Hopkinson, and D. A. King, J. Chem. Phys. **104**, 4283 (1996).
[11] K. Johnson, Q. Ge, S. Titmuss, and D. A. King, J. Chem. Phys. **112**, 10460 (2000).
[12] T. Ali, B. Klötzer, A. V. Walker, Q. Ge, and D. A. King, J. Chem. Phys. **109**, 9967 (1998).
[13] C. R. Brundle and J. Q. Broughton, in *The Chemical Physics of Solid Surfaces and Heterogeneous Catalysis*, edited by D. A. King and D. P. Woodruff (Elsevier, Amsterdam, 1990), Vol. 3A, pp. 131–388.
[14] A. Zangwill, *Physics at Surfaces* (Cambridge University Press, Cambridge, 1988).
[15] J. W. Evans, J. Chem. Phys. **87**, 3038 (1987).
[16] D.-J. Liu and J. W. Evans, Surf. Sci. **563**, 13 (2004).
[17] D.-J. Liu and J. W. Evans, J. Chem. Phys. **124**, 154705 (2006).
[18] T. Zambelli, J. V. Barth, J. Wintterlin, and G. Ertl, Nature (London) **390**, 495 (1997).
[19] D.-J. Liu, J. Phys. Chem. C **111**, 14698 (2007).
[20] D.-J. Liu and J. W. Evans, Prog. Surf. Sci. **88**, 393 (2013).
[21] C. Carbogno, A. Groß, J. Meyer, and K. Reuter, in *Dynamics of Gas-Surface Interactions: Atomic-level Description of Elementary Processes*, edited by R. D. Muiño and H. F. Busnengo (Springer, Berlin, 2012).
[22] A. K. Tiwari, S. Nave, and B. Jackson, Phys. Rev. Lett. **103**, 253201 (2009).
[23] J. Meyer and K. Reuter, New J. Phys. **13**, 085010 (2011).
[24] A. Eichler, F. Mittendorfer, and J. Hafner, Phys. Rev. B **62**, 4744 (2000).
[25] J. Behler, B. Delley, S. Lorenz, K. Reuter, and M. Scheffler, Phys. Rev. Lett. **94**, 036104 (2005).
[26] F. Libisch, C. Huang, P. Liao, M. Pavone, and E. A. Carter, Phys. Rev. Lett. **109**, 198303 (2012).
[27] R. B. Getman, W. F. Schneider, A. D. Smeltz, W. N. Delgass, and F. H. Ribeiro, Phys. Rev. Lett. **102**, 076101 (2009).
[28] D. J. Miller, H. Öberg, L.-A. Näslund, T. Anniyev, H. Ogasawara, L. G. M. Pettersson, and A. Nilsson, J. Chem. Phys. **133**, 224701 (2010).
[29] G. Kresse and J. Furthmüller, Comput. Mater. Sci. **6**, 15 (1996).
[30] J. P. Perdew, K. Burke, and M. Ernzerhof, Phys. Rev. Lett. **77**, 3865 (1996).
[31] P. E. Blöchl, Phys. Rev. B **50**, 17953 (1994).
[32] J. Neugebauer and M. Scheffler, Phys. Rev. B **46**, 16067 (1992).
[33] D.-J. Liu, Phys. Rev. B **81**, 035415 (2010).
[34] J. P. Perdew, A. Ruzsinszky, G. I. Csonka, O. A. Vydrov, G. E. Scuseria, L. A. Constantin, X. Zhou, and K. Burke, Phys. Rev. Lett. **100**, 136406 (2008).
[35] S. S. Alexandre, E. Anglada, J. M. Soler, and F. Yndurain, Phys. Rev. B **74**, 054405 (2006).
[36] A. Baraldi, V. R. Dhanak, G. Comelli, K. C. Prince, and R. Rosei, Phys. Rev. B **56**, 10511 (1997).
[37] Y. Han, B. Unal, and J. W. Evans, Phys. Rev. Lett. **108**, 216102 (2012).
[38] Y. Han, D. Jing, B. Ünal, P. A. Thiel, and J. W. Evans, Phys. Rev. B **84**, 113414 (2011).
[39] Y. Zhang, V. Blum, and K. Reuter, Phys. Rev. B **75**, 235406 (2007).
[40] M. Todorova, E. Lundgren, V. Blum, A. Mikkelsen, S. Gray, J. Gustafson, M. Borg, J. Rogal, K. Reuter, J. N. Andersen, and M. Scheffler, Surf. Sci. **541**, 101 (2003).
[41] J. W. Evans, Rev. Mod. Phys. **65**, 1281 (1993).
[42] L. Vattuone, A. Gerbi, D. Cappelletti, F. Pirani, R. Gunnella, L. Savio, and M. Rocca, Angew. Chem. Int. Ed. **48**, 4845 (2009).
[43] H. Brune, J. Wintterlin, R. J. Behm, and G. Ertl, Phys. Rev. Lett. **68**, 624 (1992).
[44] M. Schmid, G. Leonardelli, R. Tscheließnig, A. Biedermann, and P. Varga, Surf. Sci. **478**, L355 (2001).
[45] M.-F. Hseih, D.-S. Lin, H. Gawronski, and K. Morgenstern, J. Chem. Phys. **131**, 174709 (2009).